# Martensitic transformation of $Ni_2FeGa$ ferromagnetic shape-memory alloy studied via transmission electron microscopy and electron energy-loss spectroscopy

H. R. Zhang,* C. Ma, H. F. Tian, G. H. Wu, and J. Q. Li

*Beijing National Laboratory for Condensed Matter Physics, Institute of Physics, Chinese Academy of Sciences, Beijing 100080, People's Republic of China*

(Received 20 March 2008; revised manuscript received 16 May 2008; published 13 June 2008)

The structural properties of $Ni_2FeGa$ Heusler alloy synthesized by melt-spinning technique have been systematically studied by means of *in situ* heating and cooling transmission electron microscopy. It was found that the $Ni_2FeGa$ alloy was annealed into a well-defined $L2_1$ structure at around 980 K, and complex microstructural domains appeared along with lowering temperature. At room temperature (293 K), a rich variety of micromodulated domains were observed. The domain structures were aligned along the ⟨110⟩ or ⟨100⟩ directions resulting to complex tweed structures. Below martensitic transformation (MT) temperature ($M_s$, ~142 K), the cubic parent phase transformed into unmodulated martensitic variants and modulated martensitic variants. The variants were alternated along the ⟨100⟩ direction with various arrangements and steplike incommensurate boundaries. The modulated martensitic variants were composed of lamellar structures that have predominately a 5*M* modulation structure along the ⟨110⟩ directions. The electron energy-loss spectroscopy analysis of the low-loss region and the electron energy-loss near-edge fine structure revealed a visible change of the electronic structure along with MT, which can be well interpreted by means of intra-atomic or intraband charge redistribution due to *spd* orbital hybridization among the Ni-Fe-Ga atoms.

DOI: 10.1103/PhysRevB.77.214106 PACS number(s): 81.30.Kf, 68.37.Lp, 68.49.Uv, 71.20.Lp

## I. INTRODUCTION

Martensitic transformation (MT) occurs in many different metallic, ceramic, and polymeric systems and is of significant importance to understand its origin. The changes in crystallographic structure and electronic structure are critical issues of the MT. Much endeavor has been focused on these studies for a long time.[1–8] Conventional transmission electron microscopy (TEM) has been extensively employed to study the crystallographic change of the MT for more than half a century. TEM-based electron energy-loss spectroscopy (EELS), as a well-established technique, has been successfully employed to measure the small change in electronic structure of many systems such as alloys[9,10] and oxides[11,12] in the past decades. However, up to now, very few studies of EELS have been conducted on the MT.[8] In this work, EELS has been successfully employed to measure the change in electronic structure of $Ni_2FeGa$ ferromagnetic shape-memory alloys (FSMA) on MT by means of *in situ* heating and cooling TEM techniques. $Ni_2FeGa$ alloy is a high atomic order $L2_1$ structural Heusler alloy developed recently by a melt-spinning technique. This alloy has a Curie temperature of $T_c$=430 K and a martensitic transformation temperature of $M_s$=142 K. This alloy has a two-way shape-memory effect with a completely recoverable large strain of 0.3% and a low saturated magnetic field of 0.6 T, upon the MT, which make it a good candidate for applications as smart materials.[13,14] Unlike the extensively studied Ni-Mn-Ga system, Ni-Fe-Ga cannot be synthesized into $Ni_2FeGa$ Heusler alloy phase by conventional melting method because of the strong competition between disordered austenitic $\gamma$ solid solution phase and ordered $L2_1$ intermetallic phase during the solidification process. Alternately, melt-spun ribbon technique can be used to avoid the nonferromagnetic $\gamma$ solid solution phase and mainly form the ferromagnetic $L2_1$ $Ni_2FeGa$ Heusler alloy phase directly. Although powder x-ray diffraction (XRD) measurements indicated that the as-prepared $Ni_2FeGa$ alloy was well crystallized into cubic Heusler phase without the presence of other different phases,[13] there are rich variety of microstructures in the $Ni_2FeGa$ alloy synthesized by this nonequilibrium solidification method.[6] These microstructures are possibly premartensitic domains and have a great influence on the MT. In this work, various electron microscopy methods have been employed to study the microstructural and electronic structural properties of melt-spun ribbon $Ni_2FeGa$ FSMA.

## II. EXPERIMENTAL PROCEDURES

The $Ni_2FeGa$ ribbon samples were synthesized by spinning the melt of the precursor ingot with a $Ni_2FeGa$ composition, prepared by melting pure metals in proportion in an induction furnace under the argon atmosphere, onto a high-speed cooling copper wheel. Experimental details on the sample preparation and related characterization of physical properties have been reported in Ref. 13.

It is well known that thermoelastic martensites are subjected to MT under certain condition of stress and strain. In order to avoid stress introduced from the grinding during TEM sample preparation, 5-$\mu$m-thick ribbons were selected to ion-mill directly. The experiments were carried out on an FEI Tecnai F20 (200 kV) field-emission TEM equipped with a Gatan imaging filter and double-tilt high-resolution cooling (370–100 K) and heating (293–1100 K) holders. In addition, the first-principles calculation was performed by density-functional theory (DFT).

 

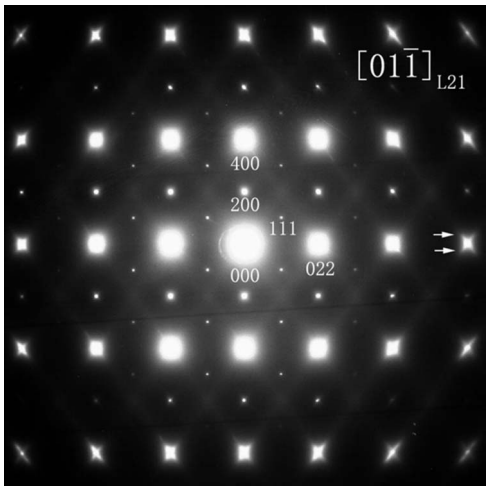


FIG. 1. SAEDP taken along the [01$\bar{1}$] zone axis, the well-defined {111} diffraction spots reveal current Ni-Fe-Ga system $L2_1$ structure feature.

## III. RESULTS AND DISCUSSION

### A. High-temperature transmission electron microscopy analysis

Heusler alloys, defined by the generic formula $X_2YZ$, are ternary, magnetic, and intermetallic compounds with next-nearest-neighbor ordering $L2_1$ crystal structure.[15] In previous works, the as-prepared $Ni_2FeGa$ sample was characterized by XRD and the {111} superlattice reflections corresponding to next-nearest-neighbor ordering of $L2_1$ structure were evidenced by a Bragg diffraction peak.[13] In TEM, the existence of any ordered structure is normally detected by the presence of superstructure diffraction spots in the selected area electron-diffraction pattern (SAEDP) along certain directions. Figure 1 shows some typical features of the [01$\bar{1}$] zone-axis SAEDP of $Ni_2FeGa$ ribbon taken at RT. The sharp {111} diffraction spots reveal the well-defined $L2_1$ atomic order phase in $Ni_2FeGa$ ribbon. The most striking feature of $Ni_2FeGa$ ribbon is the satellites superimposed diffuse streaks, as shown by the white arrows, emanating from each of the main diffraction spots along the $\langle 211\rangle^*$ directions observed from [01$\bar{1}$] zone axis and along the $\langle 110\rangle^*$ directions observed from [001] zone axis (which will be discussed in Sec. III B). In the extensively investigated Ni-Al and Ni-Mn-Ga systems, the similar feature of obvious satellites superimposed on $\langle \zeta\zeta 0\rangle^*$ diffuse streaks has been assigned as anomalous [110]-TA2 phonon branch softening along the [$\bar{1}$10] direction, resulting to structural distortion and various micromodulated domain structures in the crystal, and has been identified as a remarkable feature of the precursor of MT, i.e., premartensitic state.[4,5,16,17] In order to better understand the premartensitic state in $Ni_2FeGa$, *in situ* observation of the change in the diffuse streaks and satellites was performed in a large temperature range of 100–1100 K. The diffuse streaks and satellites are temperature sensitive and become invisible at high temperature. As shown in Fig. 2, the SAEDPs were taken along the [001] zone axis at RT, 380, 450, and 980 K. The SAEDP taken at RT [Fig. 2(a)] presents a typical average structural feature of the as-prepared sample. The white arrow illustrates the satellites with the maximum intensity at about $G \pm \langle 1/3, 1/3, 0\rangle^*$, superimposed on the $\langle 110\rangle^*$ diffuse streaks emanating from each of the main diffraction spots. Besides the $\langle 110\rangle^*$ and $\langle 211\rangle^*$ diffuse streaks emanating from the main diffraction spots, another remarkable feature observed in Ni-Fe-Ga system is

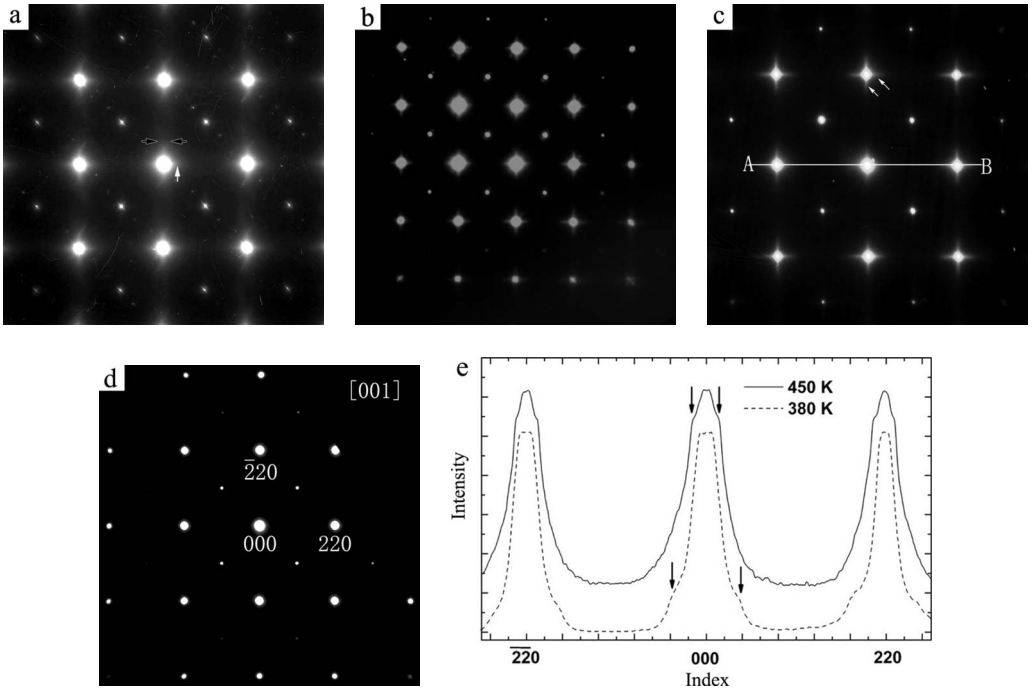


FIG. 2. [001] zone-axis *in situ* heating observation of the evolution of the $\langle \zeta\zeta 0\rangle^*$ diffuse streaks: (a) 293 K, (b) 380 K, (c) 450 K, and (d) 980 K. (e) Microphotometric density curves measured from the region of A-B indicated in (c).

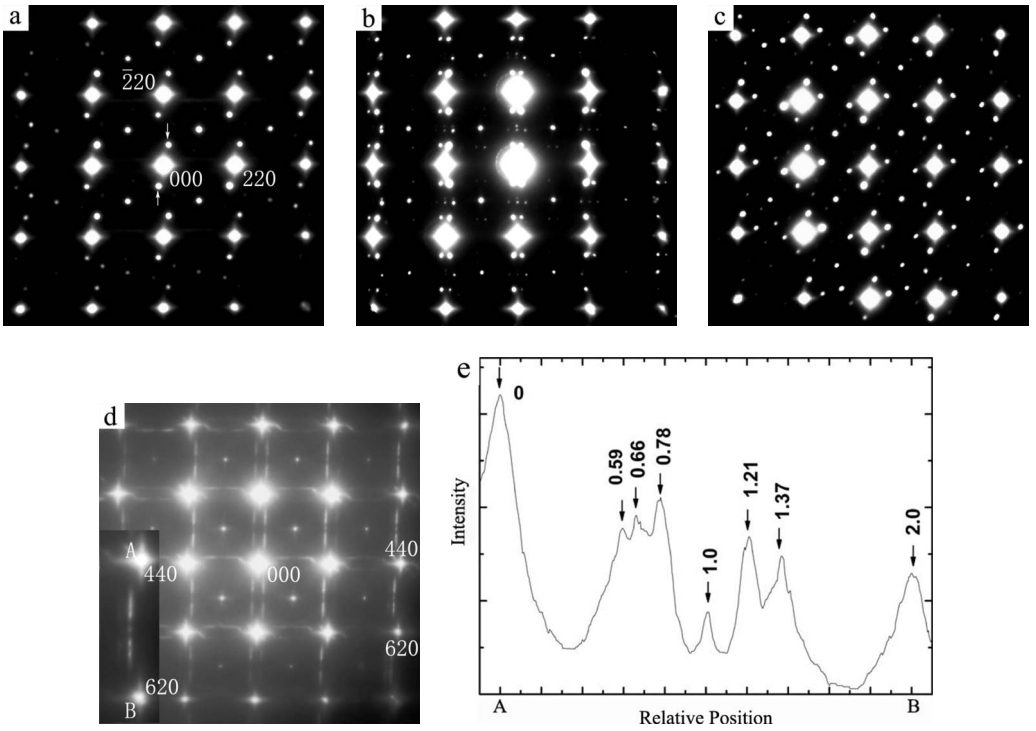


FIG. 3. [001] zone-axis SAEDP observation of the micromodulated structures in as-prepared sample at room temperature: [(a), (b), and (c)] Showing three different configurations of the TS satellites. (d) Showing paired diffuse streaks running symmetrically perpendicular to $\pm 0.16\langle 110\rangle^*$ directions. (e) Microphotometric density curve measured from the line of A-B indicated in the inset of (d).

the paired diffuse streaks, which are positioned between the main diffraction spots and symmetrically run parallel to the $\langle 110\rangle^*$ directions [indicated by black arrows in Fig. 2(a)], as is more clearly demonstrated in Fig. 3(d) and discussed in Sec. III B. The SAEDPs shown in Figs. 2(b) and 2(c) were taken at temperatures of 380 and 450 K, respectively. The microphotometric density curves [Fig. 2(e)] measured from the streaks of A-B as illustrated in Fig. 2(c) clearly indicate that the maximum intensity position of the diffuse satellites contracts with increasing temperature. As the temperature was increased to 980 K [Fig. 2(d)], the crystal structure transforms into standard $L2_1$ structure with the diffuse satellites and streaks disappearing, which suggests that the distortion related micromodulated domains were removed under high temperature. However, when the sample was cooled down, the diffuse streaks appeared again, which suggests that the micromodulated domains are temperature-dependent and possibly the precursor of the MT.

### B. Room temperature transmission electron microscopy analysis

$Ni_2FeGa$ Heusler alloy was prepared by spinning the melt onto high-speed copper wheel. The rapid cooling of hot melt resulted in vacancies, short-range order (SRO) microstructures, and some other metastable states, which exist at high temperature, possibly freezing into the $Ni_2FeGa$ average structure. Through SAEDP and diffraction contrast image observations, a rich variety of microstructures in the $Ni_2FeGa$ alloy have been revealed at RT. Figures 3(a)–3(d) present a set of typical SAEDPs frequently observed along the [001] zone axis at RT. Besides the main diffraction spots of $L2_1$ structure, some additional satellites and diffuse streaks were also observed. As indicated by the arrows in Fig. 3(a), the main diffraction spots are regularly surrounded by a variety of satellite spots and diffused reflections. These facts suggest the presence of complex superstructures and SRO microstructures in present system. This kind of SRO states illustrating the local structure properties of $Ni_2FeGa$ alloy are different from the well-known SRO discussed about diffusion controlled processes in binary disordered alloys such as $Au_4Mo$, $Au_4Cr$,[18] Cu-Pt,[19] etc., alloys. The intensities of the second-order reflections of these satellites decrease significantly, but still can be identified; however, the third-order reflections are totally suppressed, which suggests that the micromodulated domains giving rise to the satellites should be a transition state (TS) from SRO to LRO (long-range order). Sometimes two to three sets of such satellites could be observed in a single SAEDP taken from a small area. Figures 3(b) and 3(c) show two different configurations of two sets of such satellites. The satellites' positions can be well described by an additional modulation wave vector of $G=-0.44a^*+0.76b^*$, where $a^*$ and $b^*$ are the reciprocal-lattice vectors for the $L2_1$ structure. On the other hand, this satellite spots can be also assigned as $X$ fractional indices of $\pm 0.16\langle 110\rangle^*$ along the $\langle 110\rangle^*$ direction and $Y$ fractional indices of $\pm 0.6\langle \bar{1}10\rangle^*$ along the $\langle \bar{1}10\rangle^*$ direction, as clearly shown in the schematic illustration of Fig. 4(a). The spatial positions of the satellites are $\sim 15.4°$ off the $\langle 110\rangle^*$ direction, which suggests the TS forms with the micromodulation direction $\sim 15.4°$ off the $\langle 110\rangle$ direction. As mentioned above, Fig. 3(d) presents much clearer paired diffuse streaks run-

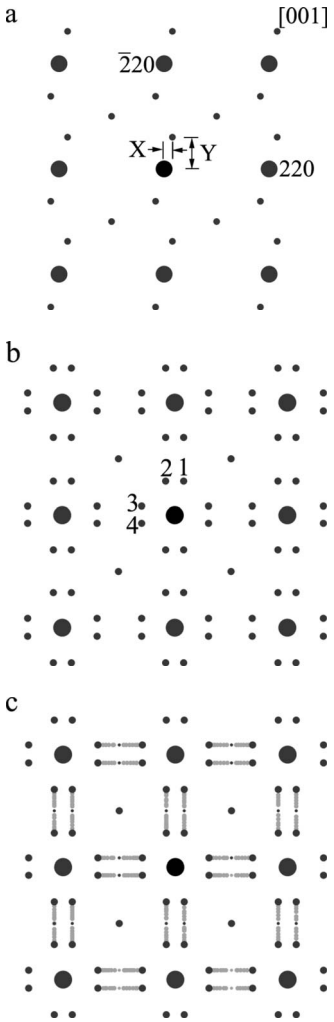


FIG. 4. Schematic reproduction of the configuration of TS satellites and paired diffuse streaks along the [001] zone axis: (a) Illustrating a single set of TS satellites positioned regularly around each of the main diffraction spots with *X* fractional indices of $\pm 0.16\langle 110\rangle^*$ and *Y* fractional indices of $\pm 0.6\langle \bar{1}10\rangle^*$. (b) Showing four possible occupation positions of the TS satellites. (c) Showing the maximum possible configuration of the TS satellites and paired diffuse streaks.

ning symmetrically perpendicular to the $G \pm 0.16\langle 110\rangle^*$ directions. The inset in the left bottom of Fig. 3(d) shows an enlarged image of the diffuse streak between $(440)^*$ and $(620)^*$ reflections. It is notable that the streak is composed of a series of diffuse satellites. The microphotometric density curve [Fig. 3(e)] measured from the line of A-B indicated in the inset of Fig. 3(d) clearly reveals the split of the diffuse streak, which suggests a multimodulated structure with different modulation wave vector *q*. It should be noted that the starting point (relative position of 0.59) and endpoint (relative position of 1.37=2−0.63) of the split should be in a symmetrical position. The little difference of 0.59 and 0.63 was arisen from Fig. 3(d) slightly off the zone axis and the Ewald sphere effect. Moreover, it is found that the starting points of the split (relative position of 0.59) are almost located at the same positions as the TS satellites (relative position of 0.60), which suggests that the multimodulated structure has a minimum modulation wave vector $q_{\min}$ (corresponding to the maximum modulation period) equivalent to the modulation wave vector of TS. This diffuse feature can be interpreted in terms of correlated $\langle 110\rangle$-axis motion of atoms, i.e., $\{110\}$ atomic displacement from the mirror planes along the $\langle 110\rangle$ axis. Evidence for this kind of atomic displacement was provided by high-resolution transmission electron microscopy (HRTEM) observation, which will be discussed in Sec. III C. The rapid solidification of hot melt which introduced vacancies and distortion into the solid, and the phonon softening along $\langle 110\rangle$ direction are possibly the causes that give rise to such an atomic displacement. In experiments, the TS satellites and the paired diffuse streaks were frequently observed to be present simultaneously in a single SAEDP with different configurations. Figure 4 shows some schematic reproductions of the configuration of satellites and paired diffuse streaks along the [001] zone axis. Figure 4(a) shows a single set of TS satellites located regularly around each of main diffraction spots with *X* fractional indices of $\pm 0.16\langle 110\rangle^*$ and *Y* fractional indices of $\pm 0.6\langle \bar{1}10\rangle^*$. Figure 4(b) shows that the TS satellites can occupy four different equivalent positions. The maximum possible configuration of the TS satellites and the paired diffuse streaks is shown in Fig. 4(c). It was noted that the TS satellites and the paired diffuse streaks were temperature sensitive. They were both disappeared by heating sample above 980 K and were appeared again by lowering the temperature.

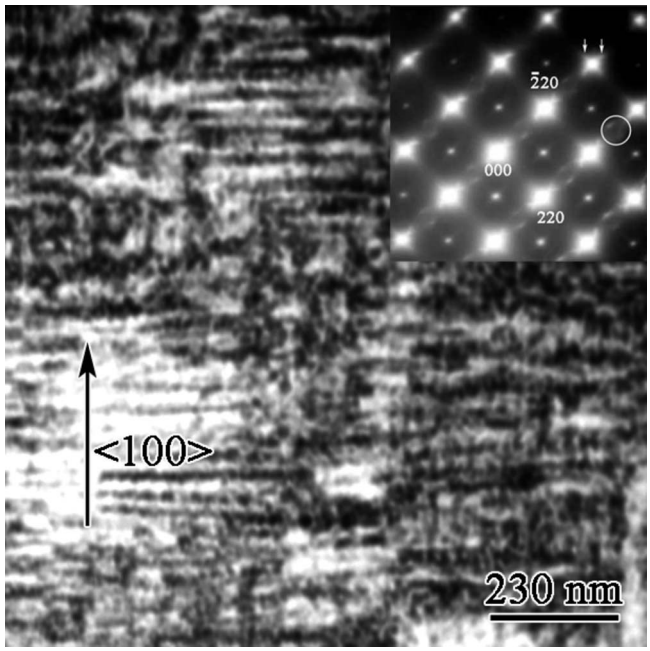


FIG. 5. A typical TEM image and corresponding SAEDP taken along [001] zone axis showing the lamella structures composed of microdomains along the $\langle 100\rangle$ direction.

The abundant SAEDPs suggest abundant microstructures existing in $Ni_2FeGa$ alloy. A rich variety of domains were observed at RT in the as-prepared samples. The well-known "tweed" structure, i.e., diffuse striations lying along the $\langle 110\rangle$ lattice directions observed in Ni-Al (Ref. 4) and Ni-Mn-Ga (Ref. 5) systems, was also observed in $Ni_2FeGa$

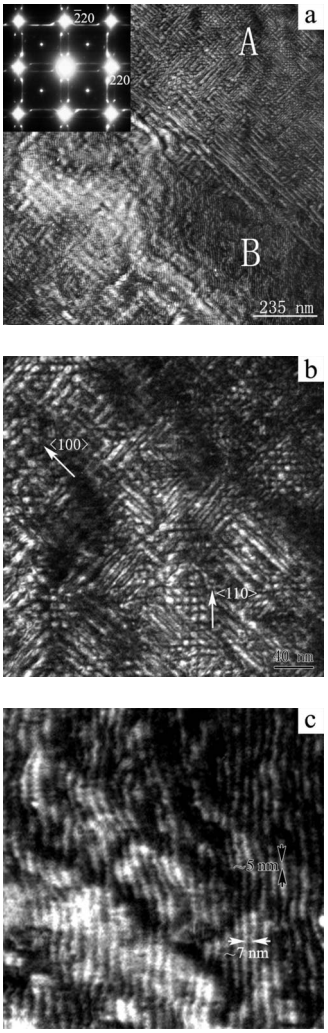


FIG. 6. (a) TEM image showing complex domain structures, the inset is the corresponding SAEDP taken along [001] zone axis. [(b) and (c)] Enlarged images of area A and area B.

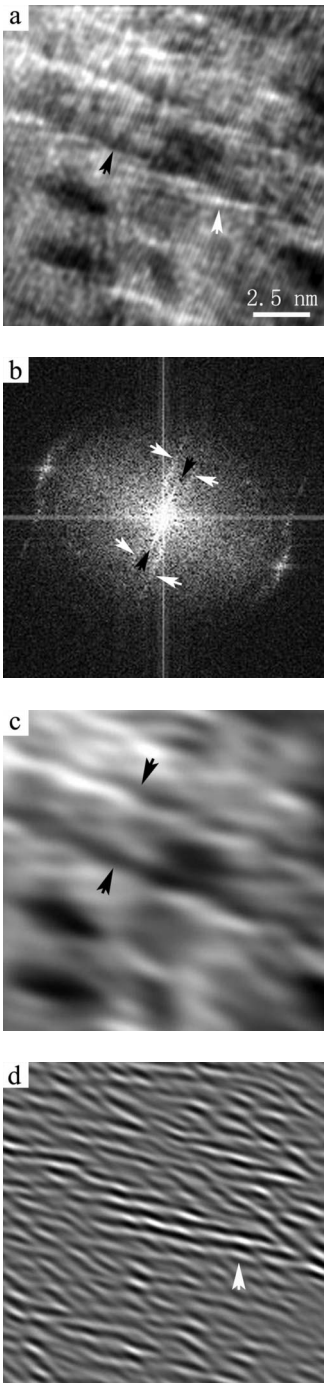


FIG. 7. (a) HRTEM image taken slightly off the [001] zone axis showing multimodulated structures and (b) corresponding FFT image; the black arrows showing short streaks emanating from the origin and the white arrows showing paired long streaks. (c) IFFT images filtered using the short streaks. (d) IFFT images filtered using the long streaks.

samples. In addition to that, some complex domain structures were also observed. As shown in Fig. 5, the lamellar structures composed of microdomains along the ⟨100⟩ directions were observed in the as-prepared samples. Since volumes of lamellar martensitic variants alternated along the ⟨100⟩ direction with habit planes of {100} were observed below the $M_s$ (which will be discussed later), the lamellar domains observed at RT possibly are precursors of the martensitic variants. Figure 6(a) shows another complex domain structure and the corresponding SAEDP, which is composed of three sets of TS satellites and two sets of paired diffuse streaks. Part of the areas A and B are enlarged and shown in Figs 6(b) and 6(c), respectively. Area A is composed of nets of microdomains of 2–10 nm along the ⟨100⟩ and/or ⟨110⟩ directions, and area B area is composed of wavy lines of microdomains of 2–5 nm along the ⟨110⟩ direction with a spacing of ~7 nm between the wavy lines. These ordered domain structures suggest a pretransformation and are possibly kinds of precursors of MT.

### C. Room temperature high-resolution transmission electron microscopy analysis

In order to better understand the abundant microstructural phenomena in $Ni_2FeGa$ alloy, HRTEM was further performed to study the details of the microstructures. Figure 7(a) shows an HRTEM image taken near the [001] zone axis.

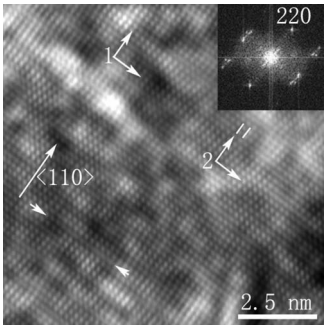


FIG. 8. [001] zone-axis HRTEM image and the corresponding FFT image; the short arrows showing stack fault and coordinates 1 and 2 illustrating a lattice shear displacement of one atom spacing every five-atom layers in area 2.

The fringes indicated by black and white arrows, respectively, suggest a coexistence of long-period and short-period multimodulated structures. Figure 7(b) is the corresponding fast Fourier transformation (FFT) image. There are short streaks emanating from the origin, indicated by the black arrows, and long paired streaks indicated by the white arrows. Figure 7(c) is the inverse fast Fourier transformation (IFFT) image filtered using the short streaks. The long-period modulation structures with slightly different modulation wavelength are clearly revealed by the fringes. Figure 7(d) is the IFFT image filtered using the long paired streaks. The fluctuation of the short rodlike fringes reveals the multimodulation and lattices distortion displacement from the average structure. It also draws a clear picture of the origin of the paired diffuse streaks, i.e., nanosized microdomains modulating along the ⟨110⟩ direction with distorted boundaries.

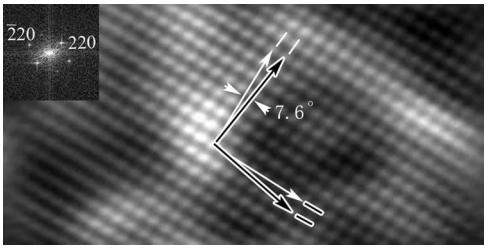


FIG. 9. A local perfect oblique lattice image cropped from one [001] zone-axis HRTEM image; the two right-angle coordinates illustrating a lattice shear displacement of one atom spacing every seven-atom layers with a 7.6° shear angle.

Figure 8 shows a [001] zone-axis HRTEM image and the corresponding FFT image. It is notable that there are plenty of stacking faults along the ⟨110⟩ direction (indicated by a pair of short arrows) and that in some local areas, the square lattices have been transformed into oblique lattices. The two right-angle coordinates indicated by 1 and 2 illustrate a lattice shear displacement of one atom spacing every five-atom layers in area 2. Figure 9 shows a local perfect oblique lattices image cropped from one [001] zone-axis HRTEM image. The two right-angle coordinates illustrate a lattice shear displacement of one atom spacing every seven-atom layers with a 7.6° shear angle. These oblique lattices suggest an obviously unmodulated monoclinic premartensitic transformation or martensitic microdomains in local areas and are possibly the precursors of the martensitic variants below $M_s$.

Figure 10(a) shows an HRTEM image of local multimodulated domains observed along the [001] zone axis. Areas 1 and 2 indicated by the dotted frames are distorted twin domains. Figures 10(b) and 10(c) are the FFT images corresponding to Fig. 10(a), areas 1 and 2, respectively. It is clear

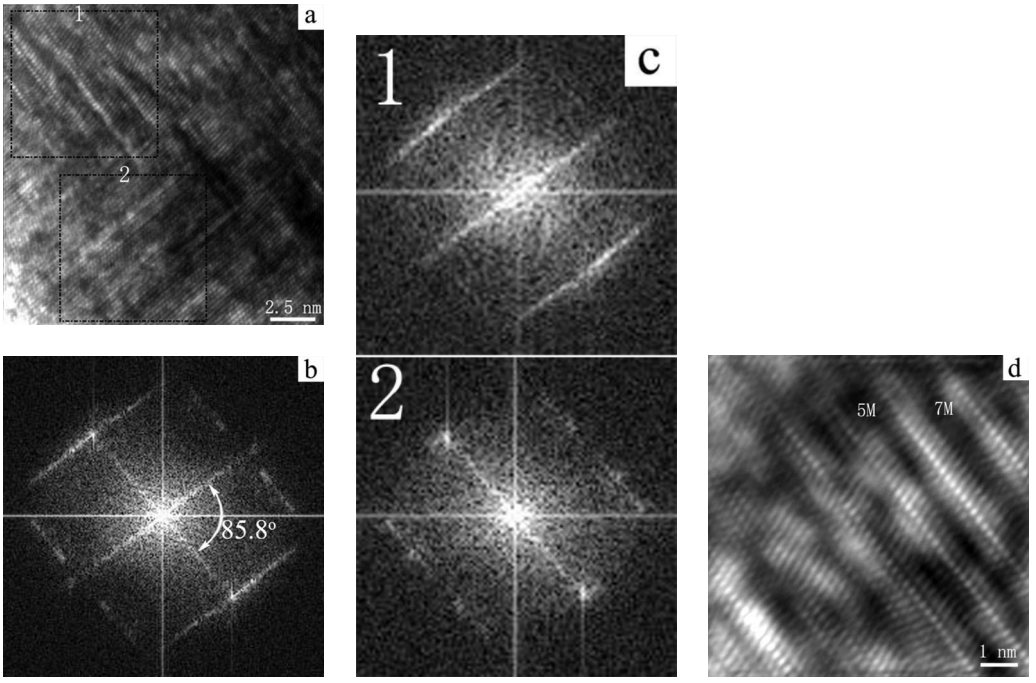


FIG. 10. (a) HRTEM image obtained at RT showing local multimodulated domains and corresponding FFT image (b). (c) FFT images corresponding to areas 1 and 2 in (a). (d) Enlarged image of area 1 showing the 5*M* and 7*M* modulation structures.

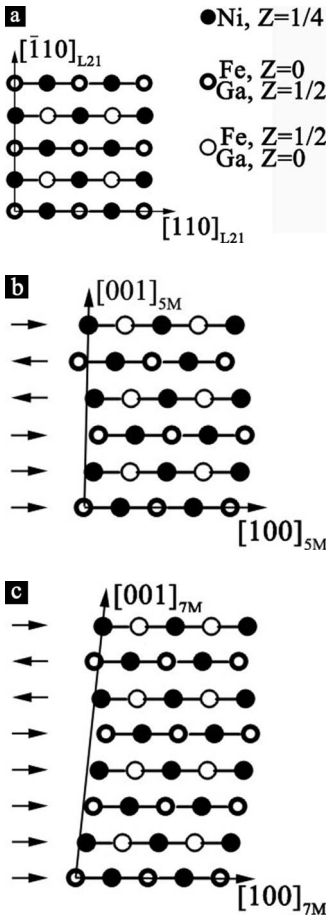


FIG. 11. Model of 5*M* and 7*M* structural transformations: (a) [001] zone-axis projection of the $L2_1$ structure; the symbol Z denoting atomic fractional coordinate along the *z* direction. [(b) and (c)] Projections of the $(3,\bar{2})$ and $(4,\bar{3})$ stacking of 5*M* and 7*M* structures, respectively; the short arrows indicating the direction of displacement of crystal planes with respect to the lower plane.

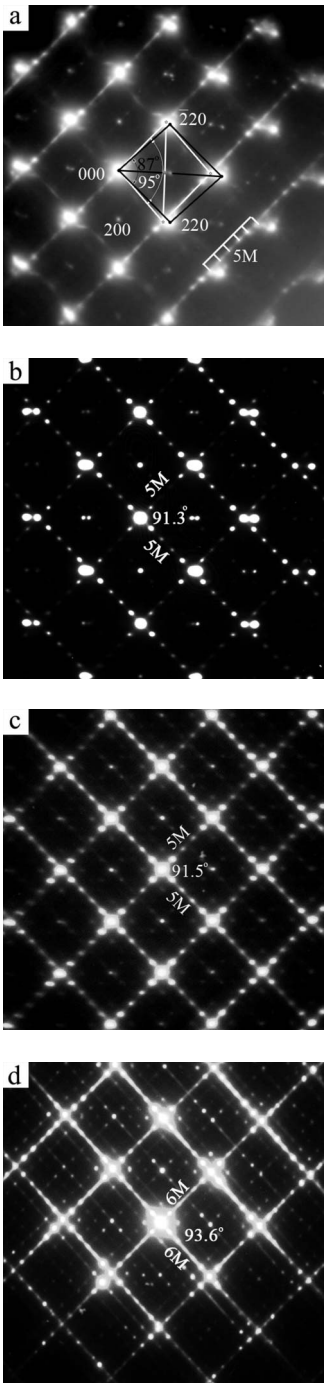


FIG. 12. SAEDP observation of the martensitic structures at 100 K: (a) Showing two sets of diffraction spots, one unmodulated and the other one 5*M* incommensurate modulated along the $\langle\bar{1}10\rangle^*$ direction. (b) Showing three sets of diffraction spots with two sets 5M incommensurate modulated and the other one set unmodulated. [(c) and (d)] Showing the unmodulated set almost coincidence with the other two sets of 5*M* and/or 6*M* incommensurate modulations, respectively.

that Fig. 10(b) is composed of two sets of diffuse streaks resulted from areas 1 and 2, respectively. As shown in Fig. 10(b), the two distorted domains are rotated 85.8° with respect to each other. Figure 10(d) is the enlarged image of area 1, which reveals an intergrowth of multimodulated structures. As shown in the image, part of the area can be defined as 5*M* and 7*M* superstructures. According to the definition of Zhdanov's notation,[20] here the 5*M* superstructure belongs to $(3\bar{2})$ stacking sequences along the $[\bar{1}10]$ direction, i.e., three $(\bar{1}10)$ planes successively displaced along the [110] direction and then two planes displaced in the opposite direction along $[\bar{1}\bar{1}0]$, and 7*M* superstructure belongs to $(4\bar{3})$ stacking sequences with four planes displaced along [110] and three planes along $[\bar{1}\bar{1}0]$. According to our study, $Ni_2FeGa$ Heusler alloy has 5*M*, 6*M*, and 7*M* structures below $M_s$. The above observed superstructures should belong to modulated martensitic domains. To better illustrate the structural transformation between the parent phase and the modulated martensitic phase, a set of model was drawn schematically in Fig. 11 in terms of the stacking of planes that undergo the primary displacement. The stacking of $(\bar{1}10)$ planes of the unmodulated cubic parent phase [Fig. 11(a)] undergoes nonhomogeneous $\{\bar{1}10\}\langle 110\rangle$ elastic shear displacement to become monoclinic 5*M* [Fig. 11(b)] or 7*M*

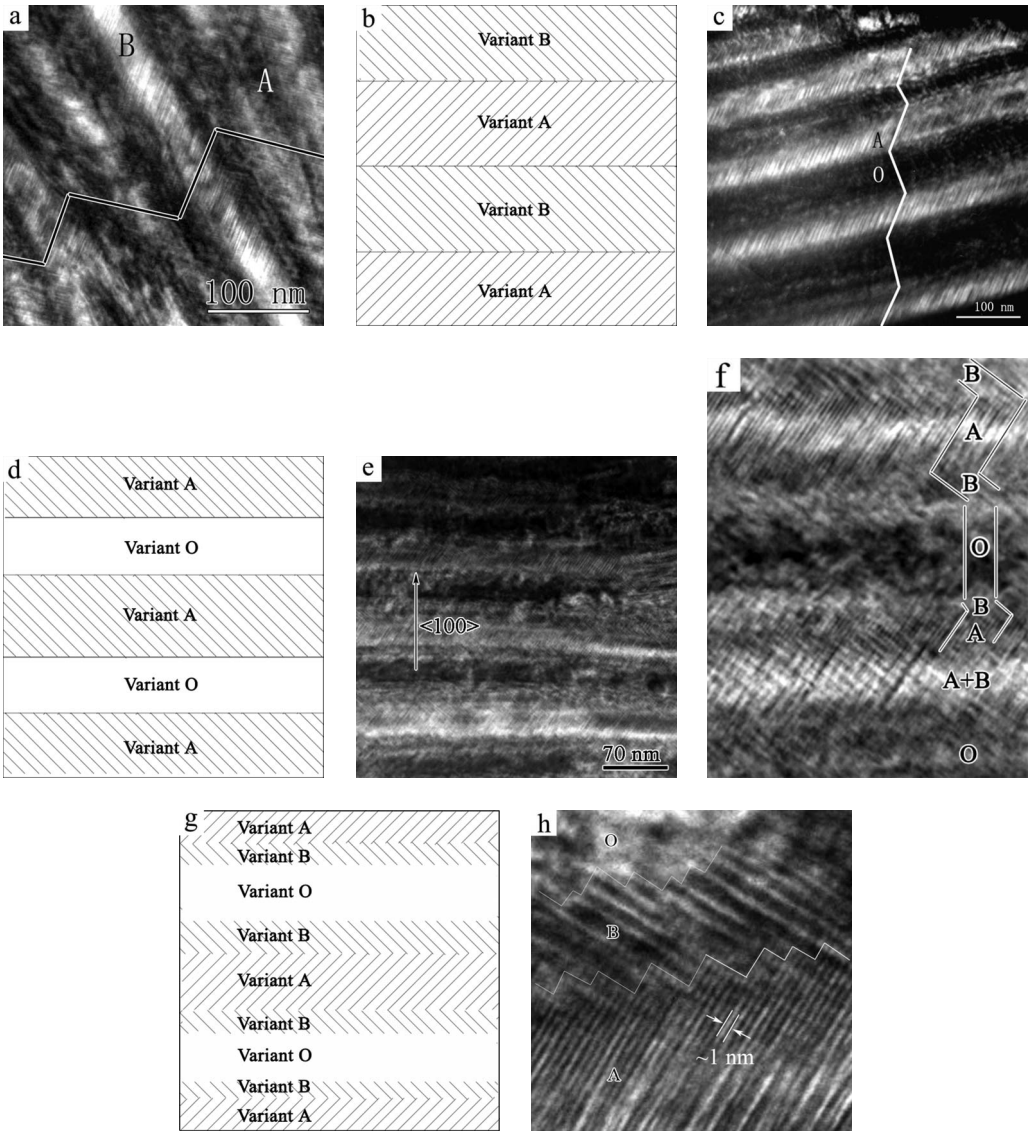


FIG. 13. HRTEM observation of martensitic variants at 100 K: [(a) and (c)] ABAB- and AOAO-type plate martensites and [(b) and (d)] corresponding schematic reproduction of the configuration of the martensitic variants, respectively. (e) BABOBABO-type plate martensites and [(f) and (g)] local enlarged image and the schematic reproduction. (h) Enlarged image showing the steplike incommensurate boundaries.

[Fig. 11(c)] martensitic structures with the $\{\bar{1}10\}_{\text{cubic}}$ planes changing to $\{001\}_{5M}$ or $\{001\}_{7M}$ planes.

The MT temperature of $Ni_2FeGa$ is about 142 K; however, from above analysis it is found that there are a rich variety of premartensitic and martensitic microdomains at RT, which make the MT mechanism of $Ni_2FeGa$ very complex. It is well known that MT is closely related to the defects such as dislocation and stacking fault which act as nucleation center for MT embryo. On the other hand, stress-strain remained in the alloy can also prompt MT.[1–4] All these imperfect factors have been observed rich in $Ni_2FeGa$ alloy and are still not enough to interpret the martensitic domains observed at RT. However, in $Ni_{50+x}Fe_{25-x}Ga_{25}$ system, it is found that the $M_s$ temperature increases with increasing Ni concentration, and the high Ni content alloy can form martensite above RT.[21] The observed martensitic domains are possibly resulted from local heterogeneous composition,[22] or spinodal decomposition,[23,24] which can also give rise to diffuse scattering and can be used to interpret well the rich and complex diffuse electron-scattering streaks in $Ni_2FeGa$ alloy.

### D. Low-temperature transmission electron microscopy analysis

In order to understand the martensitic transformation of $Ni_2FeGa$ alloy, *in situ* cooling TEM observation of cubic parent phase along [001] zone axis was performed from RT to 100 K. On cooling the sample, remarkable changes were observed below $M_s$. As shown in Fig. 12, the diffuse streaks along $\langle 110\rangle^*$ direction at RT are converted into well-defined superstructure diffraction spots at low temperature. For convenience, the diffraction spots are indexed by reference to the cubic parent phase. As indicated by black and white parallelograms, respectively, Fig. 12(a) is composed of two sets of diffraction spots. The unmodulated set likes a distorted square with an ~87° angle between the nearest two recipro-

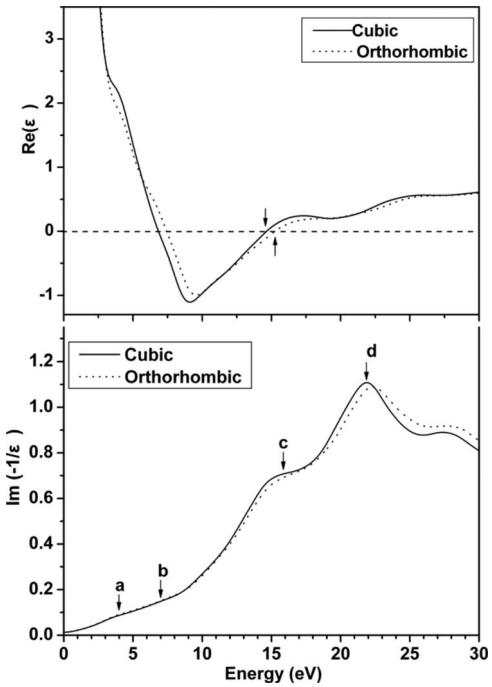


FIG. 14. Calculated real part dielectric function $\mathrm{Re}[\varepsilon(E)]$ and energy-loss function $\mathrm{Im}[-1/\varepsilon(E)]$ using unit cells of cubic parent phase and orthorhombic martensitic phase.

cal vectors, and the modulated set has a $5M$ incommensurate modulation along the $\langle\bar{1}10\rangle^*$ direction with an ~95° angle between the nearest two reciprocal vectors. Figure 12(b) shows three sets of diffraction spots with two sets $5M$ incommensurate modulated and rotated ~91.3° with respect to each other and one set unmodulated. Figures 12(c) and 12(d) show the unmodulated set of diffraction spots that almost coincide with the two sets of $5M$ and/or $6M$ incommensurate modulated diffraction spots. The weak double diffraction spots fill in the "gap" so as to produce a completely "square" pattern. The two sets of $5M$ and/or $6M$ modulated diffraction spots are rotated ~91.5° and ~93.6° with respect to each other, respectively. The incommensurate modulation diffraction can be interpreted with a monoclinic martensitic structure with $c_m^*$ axis along the $[\bar{1}10]_c^*$ modulation direction, $a_m^*$ axis along the $[110]_c^*$ direction, and $b_m^*$ axis along the $c_c^*$ direction. Since the current $Ni_2FeGa$ alloy is polycrystalline and there are 12 equivalent $\langle 110\rangle^*$ directions in cubic structure, the modulation can randomly occur in any $\langle 110\rangle^*$ direction. In TEM experiment the features of modulation structure can only be observed when the modulation planes are parallel to electron beam, which also makes the modulation direction normal to electron beam as well. However, the unmodulated set of diffraction spots observed in our system cannot be interpreted with the lattice parameters estimated for the modulated structures. Although unmodulated martensitic structures have been reported in Ni-Fe-Ga system with orthorhombic[13] or tetragonal[25] structures, the unmodulated set of diffraction spots in our system is believed to belong to a monoclinic shear martensitic structure without modulation. For convenience, here we define the martensites modulated along the $[\bar{1}10]$ and $[110]$ directions as variants A and B,

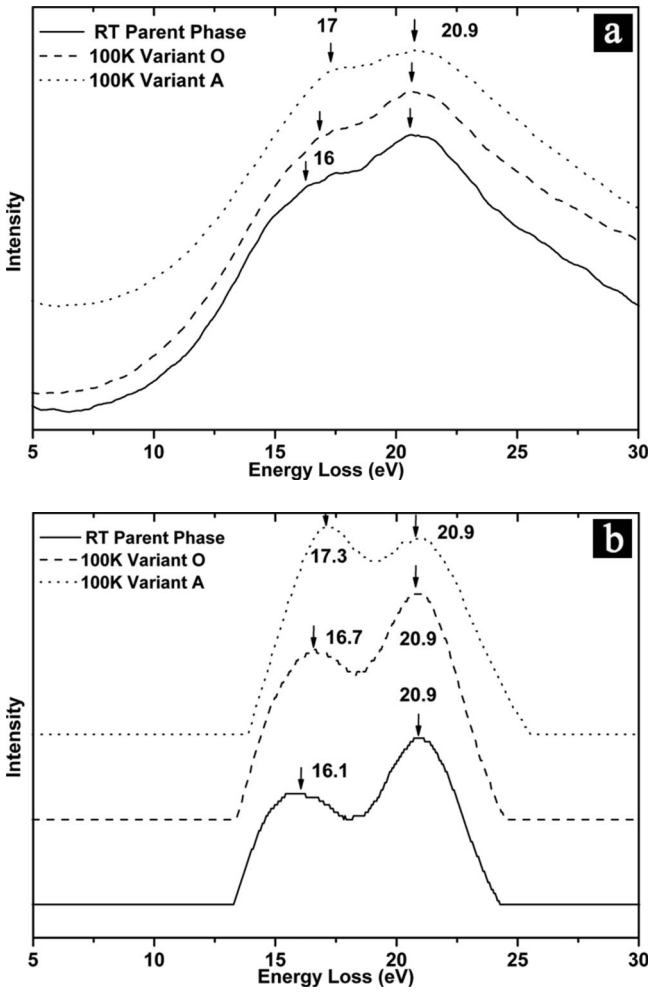


FIG. 15. (a) A typical set of low-loss spectra collected at RT on cubic parent phase, and at 100 K on variants A and O, respectively, with the dispersion setting of 0.1 eV/channel. (b) Positive component of second derivative of the spectra in (a).

respectively, and the unmodulated as variant O. If the variant O is considered as monoclinic distorted cubic and still indexed same as the cubic parent phase, it can be easily found from the diffraction patterns in Fig. 12 that variant A (variant B) and variant O have common parallel planes on $(2n,0,0)$. A crystallographic relationship between the monoclinic variant A (variant B), variant O and cubic parent phase can be deduced: $(1,0,-5)_A//(100)_O//(100)_C$, $[010]_A//[001]_O//[001]_C$. So it is apparent that the habit plane of MT is $\{100\}_C$. It should be noted that *in situ* observations on the change of the diffraction patterns in Fig. 3 have been performed. At 100 K, however, the patterns changed into one of the patterns in Fig. 12, and no difference of the microstructures (at RT) upon MT has been found.

The most obvious feature of MT is the change of morphology which reflects the crystallographic change with the MT. *In situ* HRTEM images observation from RT to 100 K was further performed to study the morphology and growth mechanism of the martensitic variants. Figures 13(a) and 13(c) show the ABAB-type and AOAO-type plate martensitic variants alternating along the $\langle 100\rangle$ direction, respectively. Figures 13(b) and 13(d) are their corresponding sche-

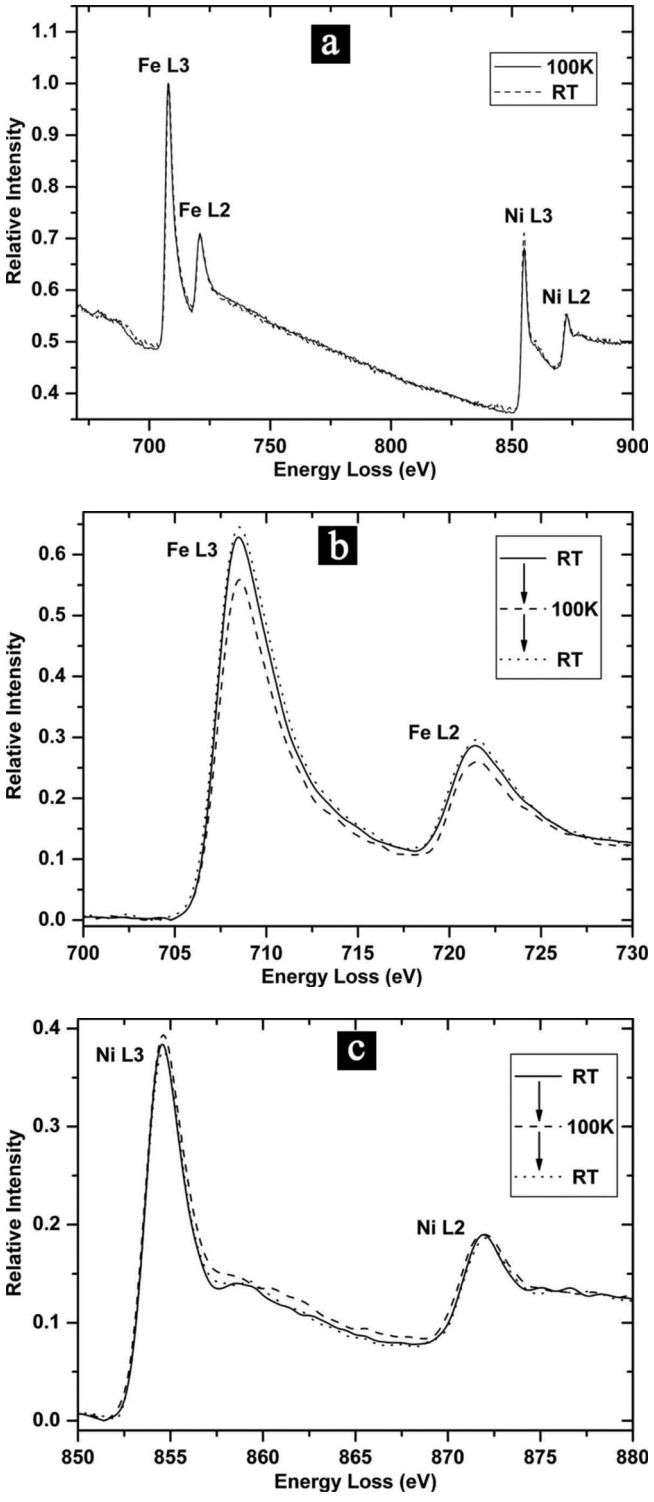


FIG. 16. (a) A typical set Fe-Ni core-loss spectra collected with 0.3 eV/channel at RT and 100 K, respectively, the spectra were aligned with the Fe $L_3$ peak at 708.5 eV and normalized with the Fe $L_3$ maximum intensity. [(b) and (c)] Two sets of Fe $L_{2,3}$ and Ni $L_{2,3}$ edges collected with 0.1 eV/channel from cubic to monoclinic to cubic reverse transformation in the same sampled area; the spectra were background subtracted and multiple scattering removed by Fourier-ratio deconvolution and then normalized by a 10 eV integration window beyond the ionization edge of 50 eV.

matic reproduction of the configuration of the martensitic variants. Variants A and B were modulated along the $[\bar{1}10]$ and [110] direction, respectively, and subdivided into nanosized lamellar modulation structures. No modulation structure can be observed in variant O. Figure 13(e) presents a BABOBABO-type plate martensitic variants alternating along the ⟨100⟩ direction. Figures 13(f) and 13(g) are the local enlarged images and the schematic reproduction of the configuration of the variants. The zigzag lines in Fig. 13(h) indicate that the intervariants boundaries are irregular steplike incommensurate structures, which are supposed to lower the boundary energy and make the structure more stable. The spacing between the lamella structures of about 1 nm width clearly evidences the $5M$ ($\sim 5d_{220}$) modulation structure. However, it should be noted that the lamella structures in local area are possibly an intergrowth of $5M$, $6M$, and $7M$.

### E. Electron energy-loss spectroscopy analysis

To study the changes of the electronic structure with the MT, theoretical calculations, and EELS measurements were performed. The electronic structure calculations were carried out using the full potential linear augmented plane-wave method within DFT, in which the exchange and correlation effects were treated using the local spin-density approximation via the WIEN2K code.[26] The $Ni_2FeGa$ cubic structure of $a=b=c=5.7405$ Å and orthorhombic structure[13] (from XRD) of $a=5.8565$ Å, $b=5.7336$ Å, and $c=5.4507$ Å were used, respectively, as parent phase and martensitic phase lattice parameters for the calculations. Figure 14 shows the calculated real part of the dielectric function $\varepsilon(E)$ and energy-loss function $\mathrm{Im}[-1/\varepsilon(E)]$, as shown in the upper and low panel, respectively. According to the part density of states, the weak peaks $a$ and $b$ in the loss function correspond to the transitions of the Ni $3d$ and Fe $3d$ states to the $4p$ states, respectively, and the strong peaks $d$ correspond to the excitations of the Ga $3d$ states to $4p$ states. The peaks $c$ can be assigned to the bulk-plasmon resonance peaks corresponding to the zero point of the dielectric function $\mathrm{Re}[\varepsilon(E)]$. It is clear that there are small blue shifts of the plasmon peaks $c$ and Ga $3d$ transition peaks $d$ with the MT, which are difficult to differentiate by EELS with 1 eV resolution.

For yielding an intrinsic change in the system, EELS spectra were collected in the same areas before and after the MT and the thicknesses of the sampled areas are about 100 nm as estimated by low-loss spectra. The energy resolution is about 1 eV measured from the full width at half maximum of the zero-loss peak. Figure 15(a) shows a series of low-loss spectra collected at RT on cubic parent phase, and at 100 K on variants A and O, respectively, with the dispersion setting of 0.1 eV/channel and acquisition time of 1 s. As shown in the experimental spectra, peaks $d$ are stable around 20.9 eV with MT, but the plasmon peaks $c$ are located in a range of 15.4–18.1 eV possibly arising from a rich variety of defects in the alloy. However, the spectra weight transfer from peak $d$ to the palsmon peak $c$ with MT can be found with the maximum at modulated variant A. As shown in Fig. 15(b), this transfer can be made more obvious by second derivative of the spectra in Fig. 15(a).

Energy-loss near-edge fine structure analyses were also performed to study the changes of electronic structure with the transformation. The theoretical calculations of Ni-Fe (Ref. 27) and Ni-Fe-Ga (Ref. 7) yielded a reduction of Fe 3*d* unoccupied state and an apparent increase of Ni 3*d* unoccupied state with MT. Moreover in the similar Ti-Ni-Fe system, the relative intensities of the Ti $L_{2,3}$ and Ni $L_{2,3}$ edges measured by EELS possess obvious changes on MT.[8] All these changes were interpreted based on a theory of charger transfer between the transition-metal elements. However, our EELS measurement of $Ni_2FeGa$ does not completely follow this rule of thumb. Figure 16(a) shows a typical set of Fe-Ni core-loss spectra collected with 0.3 eV/channel at RT and 100 K, respectively. The spectra were calibrated with the Fe $L_3$ peak at 708.5 eV and normalized with the Fe $L_3$ maximum intensity. In most of the cases, the white line intensities of Fe and Ni are scaled up or down proportionally. Moreover, the energy difference between the Fe $L_3$ and Ni $L_3$ lines are stabilized at 147 eV for over several hundreds spectra. No changes of the chemical shift and intrinsic signal intensity during the transformation were detected. Furthermore, we collected the spectra for the cubic-monoclinic-cubic transformation in the same area. The spectra were background subtracted and multiple scattering removed by Fourier-ratio deconvolution and then normalized by a 10 eV integration window beyond the ionization edge of 50 eV. Figures 16(b) and 16(c) show the Fe $L_{2,3}$ and Ni $L_{2,3}$ edges collected in the same area. The remarkable changes are the decreased intensity of the Fe $L_{2,3}$ edges collected at 100 K. This feature can be well reproduced in most of the cases independent of the collection modes, and hence supposed to be a reduction of the Fe 3*d* unoccupied state and, corresponding to a charge transfer between the alloy elements, according to the studies of charge transfer in the transition-metal alloys.[27–31] However, although there is an increase in the intensity of the Ni $L_{2,3}$ edge with the MT as shown in Fig. 16(c), the result cannot be well reproduced, as is in contrast to the prefiguration of more apparent change of Ni $L_{2,3}$ than Fe $L_{2,3}$ edges given by the calculation and experiment in Refs. 7, 8, and 27. Fortunately, there is a trend that the second peak around 8 eV above the Ni $L_3$ edge becomes broader with MT, suggesting a stronger bonding and a charge redistribution occurring in this system. So, charge transfer between Fe and Ni atoms cannot be well responsible for the changes of the Fe $L_{2,3}$ and Ni $L_{2,3}$ edges in Ni-Fe-Ga system. The intra-atomic or intraband charge redistribution due to *spd* hybridization among the Ni-Fe-Ga atoms should play an important role in the martensitic transformation with lowering symmetry.

## IV. CONCLUSION

$Ni_2FeGa$ Heusler alloy synthesized by melt-spinning technique has a rich variety of structurally micromodulated domains which are kinds of precursors of MT. At RT, the domain structures are aligned along the ⟨110⟩ or ⟨100⟩ directions resulting to complex tweed structures. A small amount of unmodulated and modulated martensitic microdomains were also observed at RT. Upon martensitic transformation below 142 K, the cubic parent phase transforms into unmodulated martensitic variants and modulated martensitic variants. The modulated martensitic variants have a lamellar structure, which is predominately a 5*M* superstructure along the ⟨110⟩ directions. The variants have a (100) habit plane and were alternated along the ⟨100⟩ directions with steplike incommensurate boundaries. The changes of the electronic structure due to *spd* hybridization and intra-atomic or intraband charge redistribution along with the MT can be observed by EELS.

## ACKNOWLEDGMENTS

This work is supported by the National Science Foundation of China, the Knowledge Innovation Project of the Chinese Academy of Sciences, and the 973 projects of the Ministry of Science and Technology of China.

*Author to whom correspondence should be addressed; hrzhang79@126.com

[1] P. C. Clapp, Phys. Status Solidi B **57**, 561 (1973).
[2] G. Guénin and P. F. Gobin, Metall. Trans. A **13**, 1127 (1982).
[3] D. Schryvers and L. E. Tanner, Ultramicroscopy **32**, 241 (1990).
[4] S. M. Shapiro, B. X. Yang, Y. Noda, L. E. Tanner, and D. Schryvers, Phys. Rev. B **44**, 9301 (1991).
[5] A. Zheludev, S. M. Shapiro, P. Wochner, A. Schwartz, M. Wall, and L. E. Tanner, Phys. Rev. B **51**, 11310 (1995).
[6] J. Q. Li, Z. H. Liu, H. C. Yu, M. Zhang, Y. Q. Zhou, and G. H. Wu, Solid State Commun. **126**, 323 (2003).
[7] Z. H. Liu, H. N. Hu, G. D. Liu, Y. T. Cui, M. Zhang, J. L. Chen, G. H. Wu, and G. Xiao, Phys. Rev. B **69**, 134415 (2004).
[8] Y. Murakami, D. Shindo, K. Otsuka, and T. Oikawa, J. Electron Microsc. **47**, 301 (1998).
[9] D. A. Muller, Phys. Rev. B **58**, 5989 (1998).
[10] P. L. Potapov, S. E. Kulkova, D. Schryvers, and J. Verbeeck, Phys. Rev. B **64**, 184110 (2001).
[11] N. D. Browning, D. J. Wallis, P. D. Nellist, and S. J. Pennycook, Micron **28**, 333 (1997).
[12] H. X. Yang, J. Q. Li, R. J. Xiao, Y. G. Shi, and H. R. Zhang, Phys. Rev. B **72**, 075106 (2005).
[13] Z. H. Liu, M. Zhang, Y. T. Cui, Y. Q. Zhou, W. H. Wang, G. H. Wu, X. X. Zhang, and G. Xiao, Appl. Phys. Lett. **82**, 424 (2003).
[14] K. Oikawa, T. Ota, T. Ohmori, Y. Tanaka, H. Morito, A. Fujita, R. Kainuma, K. Fukamichi, and K. Ishida, Appl. Phys. Lett. **81**, 5201 (2002).
[15] F. Heusler, W. Starck, and E. Haupt, Verh. Dtsch. Phys. Ges. **5**, 220 (1903).
[16] A. Planes, E. Obrado, A. Gonzalez–Comas, and L. Manosa, Phys. Rev. Lett. **79**, 3926 (1997).
[17] J. Pons, R. Santamarta, V. A. Chernenko, and E. Cesari, Mater. Chem. Phys. **81**, 457 (2003).

[18] G. Van Tendeloo and S. Amelinckx, Acta Crystallogr., Sect. B: Struct. Sci. **41**, 281 (1985).
[19] K. Ohshima and D. Watanabe, Acta Crystallogr., Sect. A: Cryst. Phys., Diffr., Theor. Gen. Crystallogr. **29**, 520 (1973).
[20] G. S. Zhdanov, Dokl. Akad. Nauk SSSR **48**, 39 (1945).
[21] Z. H. Liu, H. Liu, X. X. Zhang, M. Zhang, X. F. Duan, X. F. Dai, H. N. Hu, J. L. Chen, and G. H. Wu, Phys. Lett. A **329**, 214 (2004).
[22] P. C. Clapp, Physica D **66**, 26 (1993).
[23] Y. Ohmori and I. Tamura, Metall. Trans. A **23**, 2147 (1992).
[24] S. B. Ren, T. Tadaki, K. Shimizu, X. T. Wang, Metall. Mater. Trans. A **26**, 2001 (1995).
[25] Y. Li, J. Chen, C. Jiang, and H. Xu, Rare Metal Materials and Engineering **33**, 199 (2004).
[26] P. Blaha, K. Schwarz, G. Madsen, D. Kvasnicka, and J. Luitz, *WIEN2K, An Augmented Plane Wave Plus Local Orbital Program for Calculating Crystal Properties*, (Karlheinz Schwarz, Technical University Wien, Austria, 2001).
[27] G. Bihlmayer, R. Eibler, and A. Neckel, J. Phys. Condens. Matter **5**, 5083 (1993).
[28] D. H. Pearson, B. Fultz, and C. C. Ahn, Appl. Phys. Lett. **53**, 1405 (1988).
[29] D. H. Pearson, C. C. Ahn, and B. Fultz, Phys. Rev. B **50**, 12969 (1994).
[30] R. D. Leapman, L. A. Grunes, and P. L. Fejes, Phys. Rev. B **26**, 614 (1982).
[31] D. Shindo, K. Hiraga, A. P. Tsai, and A. Chiba, J. Electron Microsc. **42**, 48 (1993).